Bottom-Up Engineering of Peptide Cell Translocators Based on Environmentally Modulated Quadrupole Switches

Ariel Fernández,[†,‡,*] Alejandro Crespo,[†] Sridhar Maddipati,[§] and Ridgway Scott[⊥]

[†]Department of Bioengineering, Rice University, Houston, Texas 77005, [‡]Department of Experimental Therapeutics, M. D. Anderson Cancer Center, 1515 Holcombe Boulevard, Box 422, Houston, Texas 77030, [§]School of Chemical Engineering, Purdue University, West Lafayette, Indiana 47906, and [⊥]Department of Computer Science and Department of Mathematics, The University of Chicago, Chicago, Illinois 60637

ABSTRACT Designing water-soluble peptides that camouflage their polarity to cross an anhydrous phase may significantly impact drug delivery. We engineered neutrally charged peptides endowed with a conformational switch that enables them to solubilize in both water and lipid. These peptides are capable of translocating without resorting to active internalization mechanisms. Lipid solubility is induced by a quadrupolar arrangement. Our passive translocation motif possesses the highest efficiency and is derived from cellular prions.

KEYWORDS: peptide · passive translocator · conformational switch · quadrupolar arrangement · water–lipid solubility · drug delivery

Peptide-based drug carriers may offer biocompatibility advantages,[1,2] but their transportation across cell membranes remains challenging.[1–7] The current use of positively charged peptides[3] makes internalization reliant on membrane rearrangements[3,7–11] that often affect the cell integrity. Here we report on neutrally charged peptides with highly delocalized charges,[12,13] capable of minimizing hydration demands by a "camouflaging" conformational change concurrent with membrane crossing. Transference from water to lipid promotes an enhancement of intramolecular electrostatic interactions,[14] compensating for minimal dehydration penalties.[12] Our findings herald a passive and efficient translocating technology[2–4] based on peptides that translocate through a conformational switch.

Given the dual-solubility constraint, the peptides must visit two conformational ensembles, one soluble in water and the other promoting dehydration. Hence, the peptides involve polar side chains, hydrated when exposed to water but capable of engaging in intramolecular electrostatic interactions that promote internalization. Here we focus on peptides with helical (i, $i + 4$)-residue pairing. Under such constraints, an optimal translocator is shown to be found in helix 1 of the cellular prion protein.[15]

This contribution is organized as follows. First, a bottom-up computational and modeling study is presented to reveal the optimal peptide composition for translocation induced by a conformational switch. This *in silico* phase leads to the identification of the type of polar pairs transferable to an anhydrous phase with minimal desolvation penalty. Then, the predicted conformational transitions concurrent with water–lipid translocation are corroborated spectroscopically, and the peptide translocation propensity is investigated *in vitro* through a spectroscopic analysis of interfacial behavior. Finally, the translocation propensity of our prototype is investigated in cultured cells; the passive nature of the insertion event is corroborated and contrasted with the ATP-dependent transport observed for previously discovered translocators.

RESULTS AND DISCUSSION

Designing Translocators with a Conformational Switch. Peptide design requires that we identify polar pairs with enough charge delocalization to be favorably transferred to the lipid phase. Thus, we compute the free-energy change associated with a "dehydration event" made up of two contributions: (a) the work needed to strip the polar pair from surrounding water and (b) the exergonic electrostatic enhancement due to charge descreening. The dehydration is modeled by the approach of a test nonpolar sphere that expels surrounding water. Three cases are considered: an amide-carbonyl hydrogen bond, an ammonium-carboxyl (NH_4^+-COO^-) ion pair, and a guanidinium (Gd^+)-carboxyl ($(NH_2)_3C^+$-COO^-) ion pair (Figure 1). The first two

*Address correspondence to arifer@rice.edu.

Received for review September 18, 2007 and accepted December 10, 2007.

Published online December 29, 2007.
10.1021/nn700239j CCC: $40.75

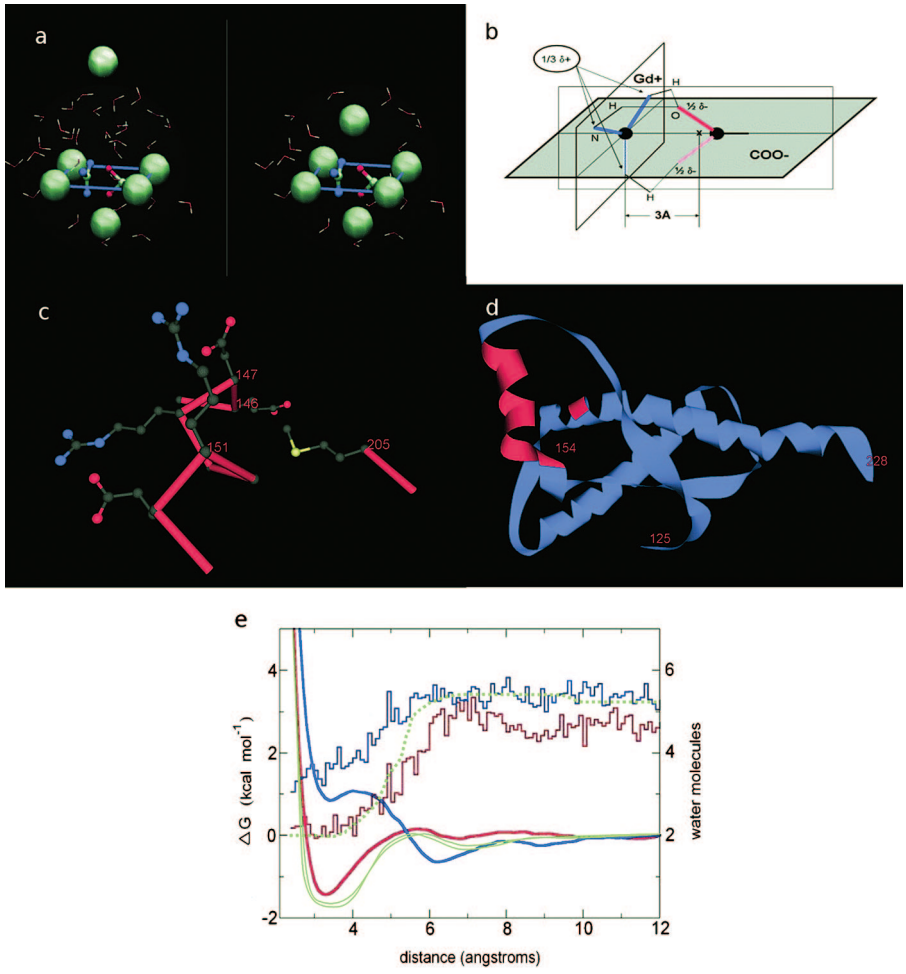

Figure 1. (a) Simulation snapshots at two stages of the wrapping process for a guanidinium-carboxyl charge pair for two values of the reaction coordinate, λ, measuring the approach by a test hydrophobe. The extent of dehydration of the electrostatic interaction is determined by placing five nonpolar balls (radius 1.7 Å) at 4.7 Å from the ion-pair center, while the test hydrophobe approaches along the principal axis of a tetragonal bypiramid (see Methods). The left panel corresponds to λ = 0.70, and the right panel corresponds to λ = 0.25. The solvation sphere in light grey has a 6.1 Å radius and is centered at the midpoint of the ion pair. The free energy change associated with dehydration of the electrostatic interaction by approach of a test hydrophobe is computed by thermodynamic integration (see Methods).[16] (b) Geometry and classical charge distribution for the guanidinium (Gd^+)-carboxylate (COO^-) pair for computational analysis of dehydration propensity. The charge baricenters are 3 Å apart. The heavy atoms (N, C, O) on both ions define two orthogonal planes. (c) Detail of the configuration of the translocator motif DRYYRE within helix 1 of the cellular prion PrP^C structure (PDB 1QM0). The ion pair from residue pair D147-R151 fits approximately the geometry specified in Figure 1b (rmsd = 0.21 Å), and the ion pair in R148-E152 fits a geometry with the ions on planes mutually orthogonal to those in Figure 1c. The position of M205 is indicated since the mutation M205R has been implicated in helix 1 destabilization. Hence, as a result of the spatial proximity, the mutation E146Q on the 145–154 prion fragment subsumes an effect of the M205R substitution. (d) Spatial location on the PrP^C structure of the 14–154 fragment, containing the translocator motif, and residue M205. (e) Free energy profile corresponding to approach by the test hydrophobe along the reaction coordinate ($0 \leq \lambda \leq 1$) for hydrogen bond (red), NH_4^+-COO^- pair (blue), and Gd^+-COO^- pair (light blue) indicated by thick lines. Also shown is the average number of water molecules within the solvation sphere (thin lines) defined in Figure 1a. The ordinates on the right indicate the number of molecules, and the ordinates on the left refer to free energies. The dehydration pattern of the Gd^+-COO^- pair (dotted line) follows that of the smaller cation (NH_4^+) when the test hydrophobe is sufficiently distant, but as the hydrophobe approaches, it switches over to the hydrogen-bond pattern. The Gd^+-COO^- pair with the conformation specified in Figure 1b has a dehydration free-energy minimum slightly lower than that of the orthogonal geometry approximated by residues R148−E152 in Figure 1c.

cases serve as controls for the more delocalized pair. Initially, the electrostatic interactions are partially dehydrated by a fixed cluster of nonpolar molecules that exclude water in all directions except the direction of approach of the test hydrophobe. Free energy changes associated with the dehydration event (Figure 1a, b, and e) were obtained from thermodynamic integration[16] on molecular dynamics simulations.[17–19]

There are significant differences in dehydration propensity for the three pairs (Figure 1e). Maximum charge delocalization in Gd^+ minimizes the dehydration penalty.[12] On the other hand, water removal enhances the Coulombic interaction,[14] making the full dehydration of the partially water-shielded Gd^+-COO^- pair the most favorable process of the three ($\Delta G = -1.71$ kcal/mol). The full dehydration of a partially water-shielded hydrogen bond is also thermodynamically favorable ($\Delta G_{HB} = -1.43$ kcal/mol), and the full dehydration of the partially shielded NH_4^+-COO^- pair is endergonic as a reult of the higher dehydration penalty associated with stripping the ammonium of its tightly bound solvation layer ($\Delta G = +0.80$ kcal/mol).[20] The dehydration level (Figure 1e) of the Gd^+-COO^- pair follows that of the NH_4^+-COO^- pair in the range $d > 6.2$ Å and the hydrogen-bond pattern for $d < 4.3$Å (d = distance between hydrophobe and polar-pair center, Figure 1a and b).

The dehydration-prone ion pairing may be incorporated into designed peptides. This requires that we take into account the inherent conformational constraints of the peptide chains dictated by the allowed regions in their torsional (Φ, Ψ)-Ramachandran maps.[21] Thus, in the absence of tertiary structure, the spatial proximity of side chains realizing the ion pairs may be achieved in the helical conformation. For this reason, a periodicity (i, $i + 4$) is adopted for the putative ion pairs. The modeling effort has been restricted to the identification of dehydration-prone ion pairs. Modeling the peptide conformational switching induced by an environmental change is extremely challenging because of the inherent difficulty in dealing with unconventional solvents and local desolvation patterns.

The dehydration propensities determined above, combined with the need for a solubility switch, impose constraints on the translocator design. Thus, the following peptides are considered: (**1**) Ac-YQDRYYRENM-NH_2, (**2**) Ac-YQDRYARENM-NH_2, (**3**) Ac-YQDRYAKENM-NH_2, and (**4**) Ac-YQDRYYKENM-NH_2. A justification of the choices is given below. The adjacency of opposite-charge aminoacids with two sets in opposite orientations eliminates charge−macrodipole interactions in the helix.[22] Peptide **1** is derived from the 145–154 fragment of helix 1 in the cellular prion (PrP^C) (PDB 1QM0),[15] after substitution E146Q. This substitution mimics the helix-1-destabilizing effect of pathogenic mutation M205R,[23] which internally titrates the wild-type E146 residue, as revealed in the structural rendering of the PrP^C (Figure 1c and d).[24]

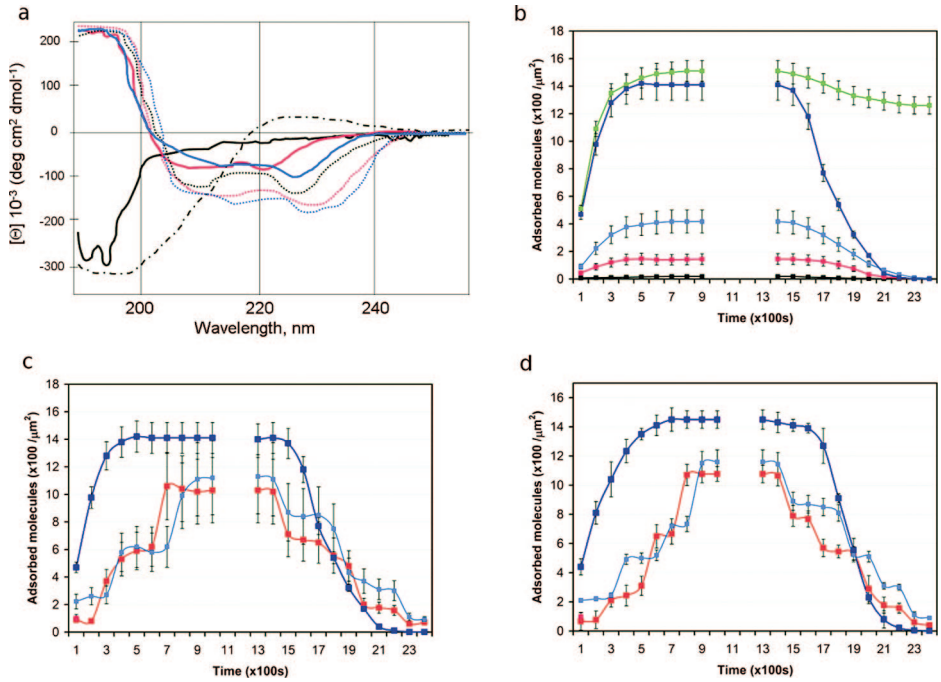

Figure 2. (a) Environmental effect on the structure ensemble of selected peptides with variable translocation potential as determined from the far-UV circular dichroism spectra. The mean residue ellipticity [Θ] for the wavelength range 180–280 nm was determined in PBS (Dulbecco's phosphate buffer saline solution, pH 7.2) and for peptides internalized in DLPC (dilauroyl phosphatidylcholine, Avanti) and DSPC (distearoyl phosphatidylcholine) liposomes. No appreciable ellipticity was detected beyond 260 nm. Ellipticity measurements in PBS are plotted in black, those in DLPC are in red, and those in DSPC are in blue. Peptide 1 (Ac-YQDRYYRENM-NH_2) is shown by solid lines, peptide 1′ (Ac-YQDEYYRRNM-NH_2) is shown by dotted lines, and peptide 1′′ (Ac-YQRRYYDENM-NH_2) is shown by hyphen/dotted lines. (b) Adsorption/desorption uptake onto a lipid phase under controlled hydrodynamic conditions determined by evanescent field spectroscopic interrogation of a DLPC Langmuir–Blodgett bilayer (see Methods). Adsorption took place at constant bulk concentration of 1.5 μM (300 K, pH7.2), and desorption occurred at 0 μM bulk concentration. The kinetics of adsorption/desorption onto and from the lipid bilayer are shown for peptides 1′ (green), 1 (purple), 2 (blue), 3 (black), and 4 (red). Error bars represent dispersions in measured uptake over five runs of each assay. On each run, measurements were made every 300 s, shifting the first measurement by 100 s in each run. A previously designed setup[27] was adapted to probe lipid penetration for the different peptides. The adsorption/desorption profiles reveal that adsorption equilibration is achieved at $t = 900$ s for all peptides. The optimal peptide for delivery across a lipid phase is one with the highest adsorption equilibrium uptake followed by the most complete desorption, as the bulk concentration is reduced from 1 to 0 μM within the 900–1400 s interval. (c) Adsorption/desorption uptake onto a DLPC (aliphatic chains length $N = 12$) bilayer revealing the translocation efficiency of peptide 1 (purple) when compared with that of vector-peptides TAT_{49-57} (orange) and $(Arg)_9$ (blue). Equilibration adsorption for peptides TAT_{49-57} and $(Arg)_9$ required 900–1000 s. Error bars represent dispersions in measured uptake over six assay runs. On each run, measurements were made every 400 s, shifting the first measurement by 100 s. (d) Adsorption/desorption uptake onto a DSPC (1,2-stearoyl-*sn*-glycero-3-phosphatidylcholine, aliphatic chains length $N = 18$, Avanti) bilayer for the same peptides indicated in Figure 2c. An identical setup and measurement schedule is adopted, and the results are displayed using the same color convention. When compared with DLPC adsorption, the dispersion in the DSPC uptake values for the positively charged peptides is significantly reduced as a result of the higher stability of the DSPC bilayer.

Interfacial Behavior of Peptide Translocators. The percentage helicities (mean residue helicity) of peptides **1**−**4** in water, as determined by signal deconvolution[22] of circular dichroism spectra,[25,26] are 24%, 22%, 19%, and 21%, respectively. The spectra for this group of peptides in water and lipid phases coincide with the one for peptide **1** shown in Figure 2a, to within an 11% confidence band. The relatively low helical content reflects the propensity of isolated polar groups to maximize hydration. Helicity increases (59%, 53%, 50%, and 53%, respectively) in DLPC liposomes, and in DSPC liposomes (61%, 57%, 50%, and 53%, respectively), in accord with the compensatory effect introduced by the enhancement of (*i*, *i* + 4)-interactions.

This behavior is contrasted with that of other engineered peptides capable of developing additional helix stabilization through charge−macrodipole interaction. Thus, peptide **1**′:Ac-YQDEYYRRNM-NH_2 shows higher helicity both in water and lipid phases (65%, 71%, and 73%, respectively), as shown in Figure 2a. This higher helicity enhances its lipid-insertion propensity but makes it a poor translocator when compared with peptide **1**, as shown below. On the other hand, peptide **1**′′: Ac-YQRRYYDENM-NH_2, with its destabilizing charge−macrodipolar interaction in the helix conformation, shows no detectable helicity in water and is insoluble in the lipid phases (Figure 2a), in accord with the high thermodynamic cost of dehydrating unpaired charges.

The absence of charge−macrodipole interaction in the designed peptides ensures low helicity in water and thus higher solubility due to charge exposure. Peptide **1** exhibits a pronounced dual solubility (Figure

2b). We quantify dual solubility from the adsorption/desorption kinetics of each peptide onto a Langmuir–Blodgett DLPC lipid bilayer (Figure 2b). An evanescent field optical sensoring[27] is adopted to interrogate an internalization layer 2 nm thick, within the lipid coating of the waveguide (see Methods). Thus, true peptide insertion/solubilization into the lipid phase is required to affect total reflection to detectable levels.[27] Because of its helix-stabilizing charge−macrodipole interaction, peptide **1**′:Ac-YQDEYYRRNM-NH_2 is more prone to pair charges and thus more hydrophobic than peptide **1**, as reflected by its adsorption/desorption kinetics (Figure 2b). Thus, peptide **1**′ internalizes with a higher uptake than peptide **1**, but the latter can translocate better between aqueous and lipid phase, as revealed by the difference in desorption kinetics between the two peptides (Figure 2b). Peptide **1**′′:Ac-YQRRYYDENM-NH_2, with its destabilizing charge−macrodipolar interaction in the helix conformation, shows no detectable adsorption, an indication that helical side chain interactions are needed for internalization. Thus, translocation requires a conformational transition yielding the quadrupolar − + + − charge distribution pattern.

Amphiphilic tyrosines were intercalated to promote cation−π interactions between arginine and the phenol quadrupole moment.[13] We determined dehydration propensities for such pairs by introducing amino acid substitutions to dissect dehydration effects.

The calculated free energies for the opposing processes of dehydration of (Gd^+-COO^-) and (NH_4^+-COO^-) ion pairs and hydration of the isolated ions are validated experimentally through mesoscopic measurements of equilibrium free energies of peptide insertion in the anhydrous phase. The latter thermodynamic parameters are accessible from the adsorption uptake data described below.

The equilibrium uptake ratio L_j/L_i for two peptides i, j, with $i < j = 1, \ldots, 4$, obtained from the adsorption assay, yields the thermodynamic parameters relevant to membrane internalization: $L_j/L_i = \exp(-\Delta\Delta G_{ji}/RT)$, where $\Delta\Delta G_{ji} = \Delta G_j - \Delta G_i$, with ΔG_j and ΔG_i being the free energy changes associated with transference to an anhydrous phase for peptides j and i, respectively. In turn, these parameters may be contrasted against the theoretical results from thermodynamic integration (Figure 1e), as shown below.

The R7K substitution (**1** → **4**) affects both the charged pair and cation−π interaction and thus may be decomposed into three successive substitutions, Y6A (**1** → **2**), R7K (**2** → **3**), and A6Y (**3** → **4**), each designed to assess the dehydration effect on a single electrostatic interaction. Thus, $\Delta\Delta G_{14} = \Delta\Delta G_{12} + \Delta\Delta G_{23} + \Delta\Delta G_{34}$. The measured adsorption uptakes at equilibrium (Figure 2a) yield $\Delta\Delta G_{12} = +0.75 \pm 0.11$ kcal/mol, $\Delta\Delta G_{23} = +2.23 \pm 0.42$ kcal/mol, and $\Delta\Delta G_{34} = -1.40 \pm 0.31$ kcal/mol, where $\Delta\Delta G_{12} \approx -\Delta G_{YR}$, $\Delta\Delta G_{23} \approx (\Delta G_{DK} - \Delta G_{DR})$, and $\Delta\Delta G_{34} \approx \Delta G_{YK}$. Here ΔG_{YR} and ΔG_{YK} are the respective free energy changes associated with transferring cation−π R-Y and K-Y pairs from water to lipid, and ΔG_{DR} and ΔG_{DK} are the changes associated with the transference of D-R and D-K ion pairs. Thus, the charge−π-cloud interaction is significantly more enhanced upon dehydration the smaller the cation size,[13] compensating for the greater amount of work needed to strip the solvation layer of the smaller cation. Hence, the internalization of the R-Y pair is less favorable than that of the K-Y pair. On the other hand, both cation-π interactions are favorably internalized (transference $\Delta G < 0$).

The difference in dehydration propensity fostered by increasing charge delocalization, $\Delta G_{DR} - \Delta G_{DK}$, is decisive in making peptide **1** the one with the highest translocation propensity, as confirmed below. The theoretical estimation gives $\Delta G_{DR} - \Delta G_{DK} = (-1.71 - 0.80)$ kcal/mol $= -2.51$ kcal/mol, comparing well with the experimental value $-\Delta\Delta G_{23} = -2.23 \pm 0.42$ kcal/mol.

It is then possible to design peptides with translocation propensity by minimizing the polar dehydration penalties, as suggested by the adsorption/desorption experiments (Figure 2b). Thus, dual-solubility peptides are subject to three constraints: (a) internal compensation of charges, (b) large charge delocalization to minimize dehydration penalties, and (c) electrostatic enhancement upon dehydration. We found a quadrupolar motif, DRYYRE, that fulfills these requirements and optimizes translocation. The R → K substitution on such motifs hinders translocation (Figure 2b), implying that charge delocalization is essential to minimize the dehydration penalty.

The translocation efficiency of peptide **1** may be contrasted with that of positively charged vector-peptides,[2,3] such as TAT_{49-57}, the 49–57 fragment of HIV-1 transcription activator protein (RKKRRQRRR), and $(Arg)_9$. These positively charged peptides are likely internalized through endocytosis.[28]

The *in vitro* adsorption/desorption uptake onto a DLPC bilayer, where no active (ATP-dependent) translocation is possible, is monitored for the three translocating peptides (Figure 2c). The membrane internalization of soluble peptide **1** is 22 ± 12% more efficient than that of Ac-$(Arg)_9$-NH_2, the most efficient translocator known to date.[2] The *in vitro* adsorption kinetics of Ac-TAT_{49-57}-$NH_2$and Ac-Arg_9-NH_2 differ from that of peptide **1** (Figure 2c); they present "plateau-avalanche" events, implying cooperative moves entailing nucleation events with significant lag times (100–300 s) followed by collective internalization. These results suggest that peptide-cations pair with negatively charged DLPC phosphates and that the polar pairs get dehydrated through aggregation nucleated on the lipid−water interface[27] prior to internalization. By contrast, peptide **1** passively inserts in the lipid phase, reaching equilibration at 900 s. The avalanche adsorption kinetics is better delineated on DSPC bilayers (Fig-

ure 2d) because the longer aliphatic chains ($N = 18$ *vs* $N = 12$ for DLPC) stabilize the adsorption interface thereby reducing uptake fluctuations.

Probing Translocation Efficiency in Cultured Cells. The translocation efficiency of peptide **1** was finally established through cell-internalization assays using fluorophore-labeled peptides with adequate controls (Figure 3a). The highest cellular incorporation occurs for peptide **1**, and our controls show no internalization of the isolated fluorophore rhodamine B.[28] On the other hand, rhodamine, with its highly delocalized positive charge, is unlikely to introduce major hydration demands that would in turn preclude the internalization of the peptide−fluorophore adduct. A major difference in the cellular translocation of peptide **1** versus TAT_{49-57} and $(Arg)_9$ emerges as the cells are subject to ATP depletion: translocation of positively charged peptides becomes hampered, whereas the treatment has only a marginal effect on peptide **1** internalization. Thus, in contrast with the positively charged translocators, peptide **1** is not likely internalized through an endocytosis-like mechanism but rather by passive diffusion. Furthermore, the subcellular localization of the internalized peptide **1** at the nuclear periphery of living[29] cells is different from that of the positively charged translocators that present nuclear (TAT_{49-57}) or cytoplasmic vesicular ($(Arg)_9$) localization (Figure 3b).

The perinuclear localization pattern of peptide **1** is not reflective of the cellular translocation mode; rather, it is indicative of the type of cellular transport within the cell. The latter involves a yet undeciphered localization code. By contrast, the passive cellular translocation mode has been unambiguously established through the ATP-depletion experiments (Figure 3a). On the other hand, the granular pattern of cellular localization is indicative of vehicle-mediated, possibly vacuole- or vesicle-related, cytoplasmic transport. This vectorial association of the molecule is likely to prevent delivery into the nucleus, given the stringent transport constraints of the latter.[30]

Translocation experiments in buffers at higher ionic strengths are likely to increase cell penetration propensity because higher charge screening decreases hydration free energies for isolated ions. Thus, the destabilization of the unbound state (water-soluble) promotes the dehydration-prone ion pairing, thereby enhancing lipid solubility.

We further tested the translocation efficacy of the quadrupole peptide coupled to therapeutically relevant cargo. Thus, we linked siRNA oligonucleotides to the peptide $C(YQDRYYRENM)_n$-NH_2, where n is chosen on the basis of the number of arginines required for internal neutralization of the negatively charged phosphates in the peptide–oligonucleotide conjugate. The oligonucleotides are derivatized through *cis*-diol substitution and *in situ* periodate-promoted oxidation into aldehydes. These derivatized oligonucleotides are subsequently conjugated with the N-terminus cystein (C) of the translocating peptide, producing a thiazolidine oligonucleotide–peptide linkage.[31] Translocation efficiency of the peptide−cargo conjugates was determined as in the experiment reported in Figure 3a,

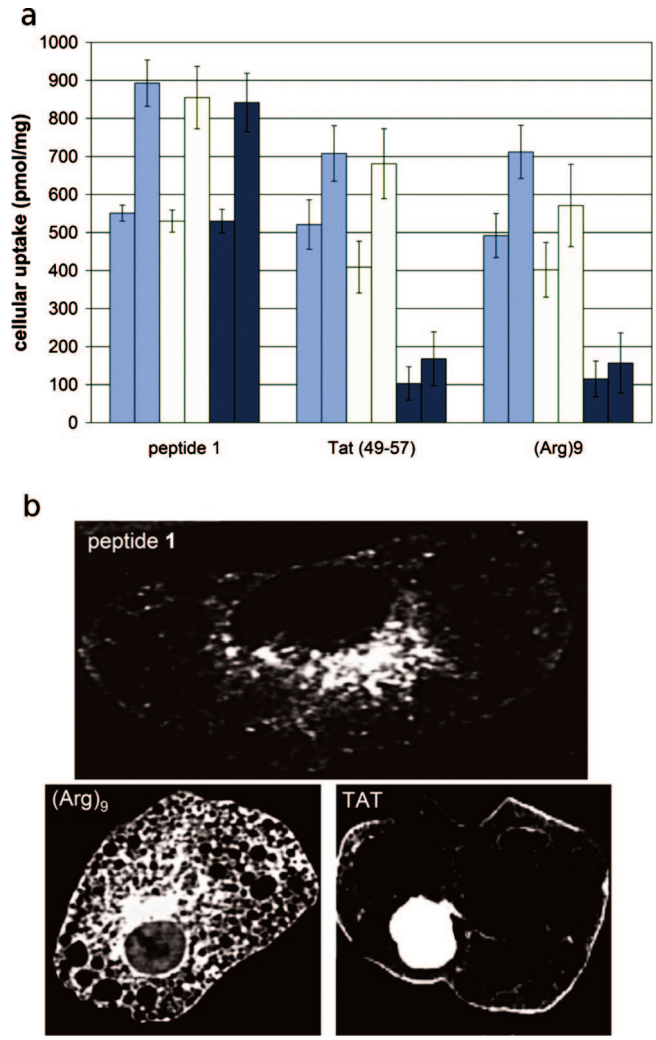

Figure 3. (a) Peptide internalization measurements revealing a higher translocation efficiency for peptide 1 over known positively charged translocators TAT_{49-57} and $(Arg)_9$. Mouse macrophage RAW264.7 cells were incubated with 1 μM fluorophore-labeled peptides for 1 and 4 h, then thoroughly washed, and lysed. Peptide internalization was assayed by fluorescent measurement on the supernatant of centrifuged cell lysate after the 1 and 4 h of peptide treatment. Error bars represent standard deviations resulting from four independent runs for each measurement. No statistically significant increase in uptake is observed after 4 h of incubation with the peptides. In controls, the isolated rhodamine fluorophore was assayed, revealing no translocation or membrane penetration. Blue bars indicate peptide uptake on cells incubated as described in Methods, yellow bars indicate uptake on cells treated with trypsin, and purple bars represents uptake on cells incubated with sodium azide (see Methods). The left-hand bar of each type corresponds to 1-h incubations with the labeled peptide, and the right-hand bar corresponds to 4-h incubations under the same conditions. Trypsin digestion enables an estimation of the extent of peptide internalization excluding membrane-bound peptides. The sodium azide treatment depletes cellular ATP, and its high impact on TAT_{49-57} and $(Arg)_9$ uptake suggests endocytosis as a dominant mechanism for internalization of these peptides, in contrast with peptide 1 internalization. (b) Cellular localization of peptide 1, TAT_{49-57}, and $(Arg)_9$ from fluorescence microscopy on living cells (see Methods).

except that internalization of thiazolidine-linked conjugates was determined from proportional counting using radioactively labeled P32-oligonucleotides. Radioactivity was measured on the supernatant of centrifuged cell lysate after 4-h treatment with the peptide−cargo conjugate at 1 μM concentration. We thus assess the translocation of siRNA for the metastasis-implicated focal adhesion kinase (FAK, target sequence 5′-AACCACCTGGGCCAGTATTAT-3′)[32] and of a control oligonucleotide with same length (5′-AATTCTCCGAACGTGTCACGT-3′) and no homology to human mRNA.[32] Although none of the thiazolidine-linked oligonucleotide conjugates with translocating peptides C(TAT_{49-57}) or C$(Arg)_9$ reveal any detectable translocation, the cellular uptake for the oligonucleotide conjugates with the oligomerized quadrupolar peptide is comparable and very significant: 108 ± 32 and 115 ± 29 pmol/mg, respectively, for FAK siRNA and control oligonucleotide.

Because our translocator is passive and not endocytotic, the peptide itself does not induce the process by triggering a response in a cellular vector (vesicle, vacuole, etc.). This makes translocation more sensitive to steric effects arising from the cargo. Further assessment of such limitations is outside the purview of this work and will be reported in future contributions.

In this work, we have designed from bottom up passive peptide translocators of high efficiency that modulate their dual solubility through conformational switches. These switches camouflage the peptide polarity in the lipid phase. We have thus validated an engineering strategy based on a minimization of dehydration costs associated with charge delocalization. The optimal design is achieved for peptides that modulate dual solubility by generating a helical quadrupole within the anhydrous phase. The technology proves to be *prima facie* more efficient than current cell-internalization technologies.

METHODS

Computation of Dehydration Free Energies. The free energy change associated with dehydration of an intramolecular electrostatic interaction by approach of a test hydrophobe is computed by thermodynamic integration following the relation[16]

$$\Delta G = \int_0^1 \frac{\partial G(\lambda)}{\partial \lambda}\, d\lambda = \int_0^1 \left\langle \frac{\partial H(\lambda)}{\partial \lambda} \right\rangle_\lambda d\lambda \qquad (1)$$

where ΔG denotes free energy change associated with the dehydration event, $H = H(\lambda)$ is the system Hamiltonian,[16,17] $0 \leq \lambda \leq 1$ is the reaction coordinate scaling with the distance d between test hydrophobe and polar pair baricenter (4.7 Å $\leq d \leq$ 12 Å), and $\langle\ \rangle_\lambda$ denotes ensemble average at a particular value of λ. The computation requires placing a dummy atom at the polar-pair center while the test hydrophobe is placed at different distances from the dummy atom. The ensemble average of $\partial H(\lambda)/\partial\lambda$ for each wrapping configuration is determined for each value of λ and integrated to yield the potential of mean force according to eq 1. Five of the total of six wrapping hydrophobes and the polar-pair atoms are kept fixed during the simulation, and the test hydrophobe is allowed to move in the direction perpendicular to the electrostatic interaction. The distance between charge baricenters and between the heavy atoms (N, O) in the hydrogen bond is fixed at 3 Å, the expected value from exhaustive examination of the PDB. The wrapping environment of the electrostatic interaction is defined by placing five hydrophobic balls (radius 1.7 Å) at 4.7 Å from the polar-pair center, while the test hydrophobe approaches along the principal axis of a tetragonal bypiramid (Figure 1a). The wrapping configuration is chosen so that the five hydrophobes at fixed positions exclude all surrounding water in the lower hemisphere of the solvation sphere (Figure 1a). The final approach by the sixth hydrophobe determines the removal of all water molecules from the microenvironment of the polar pair, defining the dehydration event. Computations are done using the GROMACS program[17] in an NVT ensemble with box size 2.5 × 2.5 × 3.5 nm^3. The electrostatics were computed by the Particle Mesh Ewald (PME) method, and a Nose-Hoover thermostat[18] was used to maintain the temperature at 300 K. A Tip3P water model with OPLS force field[19] was adopted. A total of 100 points were chosen along the reaction coordinate in the range 2−12 Å from the polar pair center. For each value of λ, the simulation was run for 150 ps, and averages were computed using the equilibrated force values from the last 100 ps. Equilibration along the λ-coordinate was sufficient to yield a state function, attested by the lack of hysteresis (within computation uncertainty) as the reaction coordinate was reversed.

Circular Dichroism. Wavelength-dependent spectra were recorded on an Aviv 62DS spectrometer (Lakewood, NJ) at the far-UV wavelength range of 180–280 nm (bandwidth = 1 nm; step interval = 0.5 nm; response time = 2 s). This individual quasi-continuous run of 400 s lies within the dispersion-based confidence band of a spectrum acquired as the average of five scans from 280 to 180 nm at lower speed (10 nm/min), sampling every 2 nm with a bandwidth of 4 nm. Measurements were performed on synthetic peptides (Sigma, >95% purity) at peptide concentration of 0.2 mM in Dulbecco's phosphate buffered saline solution (PBS, pH 7.2, DuPont de Nemours), in DLPC and in DSPC liposomes. The latter were prepared by sonication with the method of Lee et al.[25] The mean ellipticity [Θ] is given in deg cm^2/mol, and the percentage helicity was determined from the CD spectra using the method by Yang et al.[26]

Adsorption/Desorption Measurements. Peptide adsorption/desorption onto and from a Langmuir−Blodget DLPC (1,2-dilauroyl-*sn*-glycero-3-phosphatidylcholine, Avanti Polar lipids) bilayer is measured under controlled hydrodynamic conditions identical to those given in ref 27, with a constant flux of 5×10^{-3} cm^3/s. Adsorption took place at constant bulk concentration of 1.5 μM, desorption occurred at 0 μM bulk concentration, and variations in the adsorption uptake for different peptides were monitored using evanescent field total reflection spectroscopy using an optical biosensing device that interrogates a coating of an optical waveguide serving as the floor of the cell. The waveguiding TiO_2/SiO_2 coat is 180 nm thick, with a wide diffraction grating of period 412 nm (Harrick Scientific), and the evanescent field total reflection makes use of a polarized light beam with wavelength of 632.8 nm (Spectra-Physics). All measurements were made at T = 298 K and buffer composition of 10 mM Hepes/0.7 mM EDTA, pH7.1 (refractive index = 1.33303). Changes in refractive index within a layer of thickness 2 nm from the waveguide frustrate total reflection and thus become detectable, enabling a direct determination of the number of internalized peptide molecules per square micrometer.

Cell Translocation Assays. Mouse macrophage RAW264.7 cells were cultured[4] at a density of 10^5 cells/dish on 35 mm dishes. The incubation medium[4] was changed after 48 h for media containing rhodamine-labeled conjugate derivatives (Invitrogen, rhodamine B,[28] absorption wavelength 550 nm, emission wavelength 610 nm) of peptide **1**, TAT_{49-57}, and $(Arg)_9$ at 1 μM con-

centration. Incubation with the fluorophore-containing media for 1 and 4 h was followed by twice washing with PBS and final exposure to a PBS solution with 5% lysing agent Triton X-100. The lysate was centrifuged, and the fluorescence intensity of the supernatant was determined. Peptide uptake was determined on cells incubated as described above for 1 and 4 h. The uptake was also determined on cells treated with trypsin (1 mg/mL) for a 15-min digestion of labeled peptides bound to the cell membrane at the end of each incubation period and also on cells incubated with 5 mM sodium azide/10 mM 2-deoxy-D-glucose for 1 h prior to incubation with the labeled peptide solution. Trypsin digestion removes membrane-bound peptides, and the sodium azide treatment depletes cellular ATP.

Cellular Localization Assays. Mouse macrophage RAW264.7 cells were cultured as indicated above for 48 h, then the culture medium was discarded, cells were washed with NaCl/P_i solution (pH 7.3), and the cell batches were incubated with an Opti-MEM solution of rhodamine-labeled peptides at 100 nM concentration for 4 h. Subsequently, cells were rinsed three times with NaCl/P_i solution and mounted for detection of subcellular localization in living cells.[29] Cells were observed with an inverted fluorescence microscope (Olympus IX81), using 550/610 nm excitation/emission dichroic filters for the fluorophore. Critical localization differences are apparent in the fluorescence micrographs. Whereas peptide **1** is mainly distributed on the nuclear periphery, $(Arg)_9$ is located around cytoplasmic vesicles and nuclear periphery, and TAT_{49-57} is mainly concentrated in the nucleus. The cytoplasmic distribution of $(Arg)_9$ reveals that the observed cells are alive, in contrast with formaldehyde-fixed cells, which would promote a nuclear equilibrium distribution of the cationic peptide, dragged by the electrostatic attraction of polyanionic nucleic acids.[29]

Acknowledgment. The research of A.F. is supported by NIH grant 1R01 GM072614 (NIGMS) and by the John and Ann Doerr Fund for Computational Biomedicine (Program BC4R 2005).

Note added after ASAP publication: After this paper was published ASAP December 29, 2007, changes were made in a mathematical expression in the text following eq 1. The corrected version was published January 22, 2008.

REFERENCES AND NOTES

1. Marx, V. Watching peptide drugs grow up. *Chem. Eng. News* **2005**, *83*, 17–24.
2. Wender, P. A.; Mitchell, D. J.; Pattabiraman, K.; Pelkey, E. T.; Steinman, L.; Rothbard, J. B. The design, synthesis and evaluation of molecules that enable or enhance cellular uptake: peptoid molecule transporters. *Proc. Natl. Acad. Sci. U.S.A.* **2000**, *97*, 13003–13008.
3. Zorko, M.; Langel, U. Cell-penetrating peptides: mechanism and kinetics of cargo delivery. *Adv. Drug Delivery Rev.* **2005**, *57*, 529–545.
4. Futaki, S.; Suzuki, T.; Ohashi, W.; Yagamhemi, T.; Tanaka, S.; Ueda, K.; Sugiura, Y. An abundant source of membrane-permeable peptides having potential as carriers for intracellular protein delivery. *J. Biol. Chem.* **2001**, *276*, 5836–5840.
5. Binder, H.; Lindblom, G. A molecular view on the interaction of the Trojan peptide penetratin with the polar interface of lipid bilayers. *Biophys. J.* **2004**, *87*, 332–343.
6. Lensink, M. F.; Christiaens, B.; Vandekerckhove, J.; Prochiantz, A.; Rosseneu, M. Penetratin-membrane association: W48/R52/W56 shield the peptide from the aqueous phase. *Biophys. J.* **2005**, *88*, 939–952.
7. Lundberg, M.; Johansson, M. Positively charged DNA-binding proteins cause apparent cell membrane translocation. *Biochem. Biophys. Res. Commun.* **2002**, *291*, 367–371.
8. Dormitzer, P. R.; Nason, E. B.; Prasad, B. V.; Harrison, S. C. Structural rearrangements in the membrane penetration protein of a non-enveloped virus. *Nature* **2004**, *430*, 1053–1058.
9. Kämper, N.; Day, P. M.; Nowak, T.; Selinka, H.-C.; Florin, L.; Bolscher, J.; Hilbig, L.; Schiller, J. T.; Sapp, M. A. Membrane-destabilizing peptide in capsid protein L2 is required for egress of papillomavirus genomes from endosomes. *J. Virol.* **2006**, *80*, 759–768.
10. Zhang, W.; Smith, S. O. Mechanism of penetration of Antp(43–58) into membrane bilayers. *Biochemistry* **2005**, *44*, 10110–10118.
11. Lee, M.-T.; Hung, W. -C.; Chen, F. -Y.; Huang, H. W. Many-body effect of antimicrobial peptides: On the correlation between lipid's spontaneous curvature and pore formation. *Biophys. J.* **2005**, *89*, 4006–4016.
12. Mason, P. E.; Neilson, G. W.; Dempsey, C. E.; Barnes, A. C.; Cruickshank, J. M. The hydration structure of guanidinium and thiocyanate ions: Implications for protein stability in aqueous solution. *Proc. Natl. Acad. Sci. U.S.A.* **2003**, *100*, 4557–4561.
13. Mecozzi, S.; West, A. P.; Dougherty, D. A. Cation-π interactions in aromatics of biological and medicinal interest: Electrostatic potential surfaces as a useful qualitative guide. *Proc. Natl. Acad. Sci. U.S.A.* **1996**, *93*, 10566–10571.
14. Despa, F.; Fernández, A.; Berry, R. S. Dielectric modulation of biological water. *Phys. Rev. Lett.* **2004**, *93*, 228104.
15. Ziegler, J.; Sticht, H.; Marx, U. C.; Mueller, W.; Roesch, P.; Schwarzinger, S. CD and NMR studies of prion protein (PrP) helix 1. *J. Biol. Chem.* **2003**, *278*, 50175–50181.
16. Kollman, P. A. Free energy calculations: Applications to chemical and biochemical phenomena. *Chem. Rev.* **1993**, *93*, 2395–2417.
17. Lindahl, E.; Hess, B.; Van der Spoel, D. GROMACS 3.0: A package for molecular simulations and trajectory analysis. *J. Mol. Model.* **2001**, *7*, 302–317.
18. Hoover, W. G. Canonical dynamics: Equilibrium phase-space distribution. *Phys. Rev. A* **1985**, *31*, 1695–1697.
19. Rizzo, R. C.; Jorgensen, W. L. OPLS All-atom model for amines: Resolution of the amine hydration problem. *J. Am. Chem. Soc.* **1999**, *121*, 4827–4836.
20. Hendsch, Z. S.; Tidor, B. Do salt bridges stabilize proteins? A continuum electrostatic analysis. *Protein Sci.* **1994**, *3*, 211–226.
21. Voet, D.; Voet, J. G. *Biochemistry*, 3rd ed.; John Wiley & Sons Inc.: New York, 2004; pp 221–223.
22. Huyghues-Despointes, B. M.; Scholtz, J. M.; Baldwin, R. L. Helical peptides with three pairs of Asp-Arg and Glu-Arg residues with different orientations and spacings. *Protein Sci.* **1993**, *2*, 80–85.
23. Hirschberger, T.; Stork, M.; Schropp, B.; Winklhofer, K.; Tatzelt, J.; Tavan, P. Structural instability of the prion protein upon M205S/R mutations revealed by molecular dynamics simulations. *Biophys. J.* **2006**, *90*, 3908–3918.
24. Zahn, R.; Liu, A.; Luhrs, T.; Riek, R.; von Schroetter, C.; Lopez Garcia, F.; Billeter, M.; Calzolai, L.; Wider, G.; Wuthrich, K. NMR solution structure of the human prion protein. *Proc. Natl. Acad. Sci. U.S.A.* **2000**, *97*, 145–150.
25. Lee, S.; Yoshitomi, H.; Morikawa, M.; Ando, S.; Takiguchi, H.; Inoue, T.; Sugihara, G. Homooligopeptides composed of hydrophobic amino acid residues interact in a specific manner by taking α helix or beta-structure toward lipid bilayers. *Biopolymers* **2005**, *36*, 391–398.
26. Yang, J. T.; Wu, C. S.; Martinez, H. M. Calculation of protein conformation from circular dichroism. *Methods Enzymol.* **1986**, *130*, 208–269.
27. Fernández, A.; Berry, R. S. Proteins with hydrogen-bond packing defects are highly interactive with lipid bilayers: Implications for amyloidogenesis. *Proc. Natl. Acad. Sci. U.S.A.* **2003**, *100*, 2391–2396.
28. Du, H.; Fuh, R. A.; Li, J.; Corkan, A.; Lindsey, J. S. PhotochemCAD: A computer-aided design and research tool in photochemistry. *Photochem. Photobiol.* **1998**, *68*, 141–142.
29. Richard, J. P.; Melikov, K.; Vives, E.; Ramos, C.; Verbeure, B.; Gait, M. J.; Chernomordik, L.; Lebleu, B. Cell penetrating peptides: a re-evaluation of the mechanism of cell uptake. *J. Biol. Chem.* **2003**, *278*, 585–590.

30. Alberts, B.; Johnson, A.; Lewis, J.; Raff, M.; Roberts, K.; Walter, P. *Molecular Biology of the Cell*, 4th ed.; Taylor and Francis: New York, 2002; pp 669–671.
31. Zatsepin, T. S.; Stetsenko, D. A.; Arzumanov, A. A.; Romanova, E. A.; Gait, M. J.; Oretskaya, T. S. Synthesis of peptide-oligonucleotide conjugates with single and multiple peptides attached to 2′-aldehydes through thiazolidine, oxime, and hydrazine linkages. *Bioconjugate Chem.* **2002**, *13*, 822–830.
32. Halder, J. B.; Kamat, A. A.; Landen, C. N.; Han, L. Y.; Lutgendorf, S.; Lin, Y. G.; Merritt, W. M.; Jennings, N. B.; Chavez-Reyes, A.; Coleman, R. L. Focal adhesion kinase targeting for therapy of ovarian carcinoma using in vivo siRNA delivery in neutral liposomes. *Clin. Cancer Res.* **2006**, *12*, 4916–4924.